EARTH SURFACE PROCESSES AND LANDFORMS
Earth Surf. Process. Landforms **39**, 1822–1832 (2014)

Published online 10 April 2014 in Wiley Online Library
(wileyonlinelibrary.com) DOI: 10.1002/esp.3570

How do sediment yields from post-wildfire debris-laden flows depend on terrain slope, soil burn severity class, and drainage basin area? Insights from airborne-LiDAR change detection

Jon D. Pelletier* and Caitlin A. Orem
Department of Geosciences, University of Arizona, Tucson, AZ, USA

Received 5 February 2013; Revised 11 March 2014; Accepted 12 March 2014

*Correspondence to: Jon D. Pelletier, Department of Geosciences, University of Arizona, Gould-Simpson Building, 1040 East Fourth Street, Tucson, AZ 85721–0077, USA. E-mail: jdpellet@email.arizona.edu

ESPL
Earth Surface Processes and Landforms

ABSTRACT: We derived a high-resolution, spatially continuous map of erosion and deposition associated with the debris-laden flows triggered by the 2011 Las Conchas wildfire and subsequent rainstorms over a 197 km^2 area in New Mexico, USA. This map was produced using airborne-LiDAR-derived bare-earth digital elevation models (DEMs) acquired approximately one year before and one year after the wildfire. Differencing of the pre-wildfire and post-wildfire-and-rainstorm bare-earth DEMs yielded a DEM-of-difference (DoD) map that quantifies the magnitude of ground-surface elevation changes due to erosion/deposition within each 1 m^2 pixel. We applied a 0.3 m threshold filter to our DoD to remove changes that could have been due to artifacts and/or imperfect georeferencing. The 0.3 m value for the threshold filter was chosen based on the stated accuracy of the LiDAR as well as a comparison of areas of significant topographic change mapped in aerial photographs with those predicted using a range of candidate threshold values for the DoD filter. We developed an automated procedure that accepts the DoD map as input and computes, for every pixel in the DEM, the net sediment volume exported through each pixel by colluvial and/or fluvial processes using a digital routing algorithm. An analysis of the resulting sediment volume map for the Las Conchas fire demonstrates that sediment volume is proportional to upstream contributing area. After normalized by contributing area, the average sediment yield (defined as the sediment volume divided by the contributing area) increases as a power-law functions of the average terrain slope and soil burn severity class (SBSC) with exponents equal to approximately 1.5. Our analysis quantifies the relationships among sediment yield, average terrain slope, and average soil burn severity class at the watershed scale and should prove useful for predicting the geomorphic response of wildfire-affected drainage basins. Copyright © 2014 John Wiley & Sons, Ltd.

KEYWORDS: post-wildfire erosion; LiDAR; Valles Caldera

Introduction and Motivation

Recent intense droughts and a century of wildfire suppression are driving record-setting large-area and high-severity wildfires across western North American forests (Keane *et al.*, 2002; Westerling *et al.*, 2006; Miller *et al.*, 2009) and the world (Allen *et al.*, 2010). Climate models agree that warming and the associated increase in potential evapotranspiration will result in more negative water balances in many semi-arid regions, further increasing the potential for enhanced wildfire frequency and severity in the future (Williams *et al.*, 2010). In order to accurately assess potential soil loss, hazards to infrastructure, and impacts to water quality associated with this increase in wildfire activity, methods that accurately predict and measure post-wildfire sediment yields are urgently needed (Loomis *et al.*, 2003; Cannon *et al.*, 2010; Rhoades *et al.*, 2011).

In June and July, 2011, 630 km^2 of the Jemez Mountains region was burned by the Las Conchas wildfire, then the largest wildfire in New Mexico state history. The fire and subsequent monsoon-season thunderstorms resulted in extreme hydrogeomorphic changes. Prior to the fire, some piedmonts had no active channels and were entirely grass-covered (Figure 1A). A single thunderstorm on August 3, 2011 formed a ~1 km-long, gravel-dominated distributary-channel system that transported boulders up to 1 m in diameter (Figure 1B). Many drainage basins in the burned area responded similarly, if not all as dramatically, to the fire and subsequent rainstorm events. Given the extreme hydro-geomorphic changes observed after the wildfire and subsequent rainstorms in addition to the availability of high-quality airborne LiDAR (light detection and ranging) data acquired before the wildfire, the Las Conchas event provides an excellent opportunity to test the ability of repeat airborne LiDAR data to quantify the geomorphic response to wildfire and subsequent rainstorms.

The purpose of this paper is to assess the ability of airborne laser swath mapping (ALSM) acquired before and after a wildfire and subsequent rainstorms to map erosion/deposition and sediment yields in a spatially continuous manner and at high

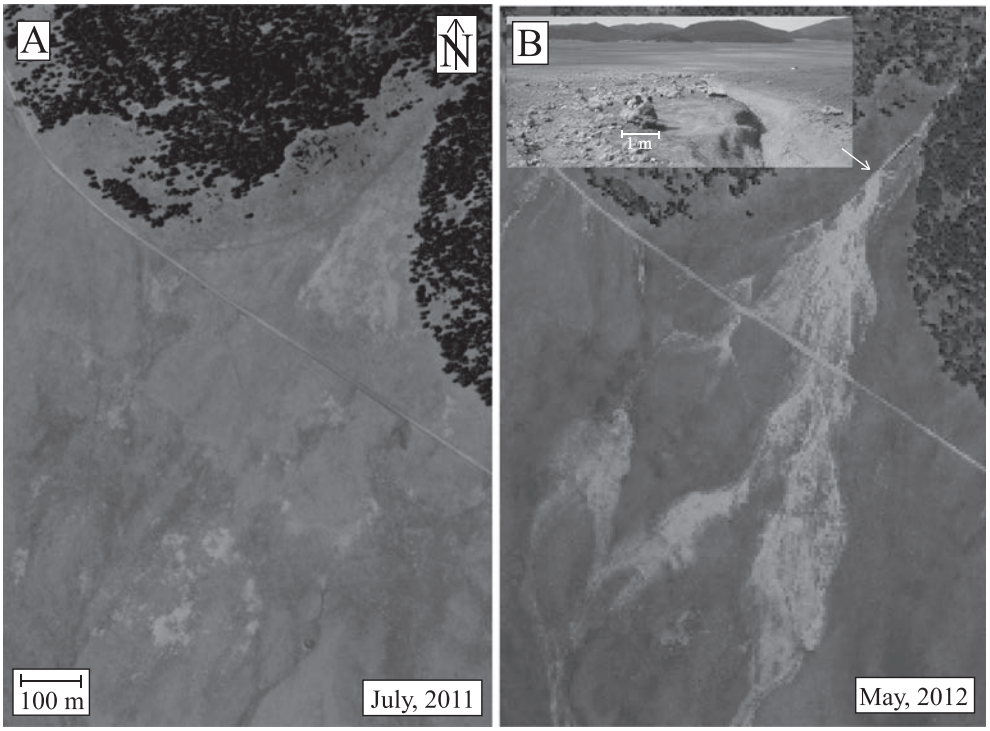

Figure 1. Example of the extreme hydro-geomorphic changes that occurred following the Las Conchas wildfire of July, 2011. Aerial photographs of a piedmont draining the south flank of Cerro del Medio in the Valles Caldera (A) before and (B) after the wildfire, illustrating the development of a new, 1-km-long, gravel-dominated distributary-channel system and associated debris-laden-flow deposit between July, 2011 and May, 2012. Eyewitness accounts constrain the origination of this channel system to a storm on August 3, 2011.

resolution over a large area (i.e. ~100 km^2). Before evaluating the potential of this method, it is appropriate to identify the standard method(s) now used for quantifying post-fire erosion/deposition and sediment yields. One standard method for quantifying erosion/deposition and the volume of sediment exported from drainage basins associated with post-wildfire erosion is to survey cross-sectional profiles following the wildfire and subsequent rainstorms and, assuming that a V-shaped cross-section (or some other appropriate shape based on the cross-sectional shape of nearby un-incised valley bottoms) existed prior to the wildfire, project the gradients of the valley-bottom-bounding hillslopes into the eroded valley bottom to construct a V-shaped pre-event valley-bottom cross-section. This assumed pre-event cross-section is used, in conjunction with the measured post-event cross-section, to estimate the change in cross-sectional area at multiple locations along longitudinal profiles (Gartner *et al.*, 2008; Cannon *et al.*, 2010). This technique assumes that the volumes of material scoured from valley bottoms within a drainage basin can be summed to estimate the volume of sediment emanating from those drainage basins. Sediment volumes estimated in this way can be divided by the contributing area of the drainage basin to estimate a sediment yield (defined as the exported sediment volume per unit area per unit time) associated with post-fire erosion. This method has provided valuable information but it has limitations. First, uncertainty is introduced by assuming the shape of the pre-wildfire cross-section and considering scour only (i.e. neglecting deposition) in estimating the volume of exported sediment. Second, field-based survey methods cannot provide a high-resolution, spatially continuous map of post-wildfire sediment yields over a large area. A second standard method for quantifying post-wildfire sediment yields is to use the sediment deposited in traps. While sediment traps are useful, they provide sediment yield measurements at only a small number of locations where sediment traps are located. In this paper, we test the ability of ALSM to provide high-resolution, spatially continuous maps of erosion and deposition over a large area. We also propose and evaluate a new raster-based method for computing the volume of sediment exported for drainage basins based on a digital elevation model (DEM)-of-difference (DoD) map obtained by differencing of pre- and post-event LiDAR data.

Study Site Description and Post-wildfire Field Observations

Our study area includes the portion of the Las Conchas burned area within the Valles Caldera National Preserve (VCNP) and a portion of the adjacent Bandelier National Monument (Figure 2A) within the Jemez Mountains region. The VCNP is located at the site of a caldera formed 1.25 Ma (Figure 2) (Goff *et al.*, 2006). Elevations range from 2300 in the lower grasslands to 3432 m at the summit of the Redondo Peak resurgent dome. Parent material at the site is mostly rhyolite with some sedimentary and volcaniclastic deposits (Goff *et al.*, 2006). The forested uplands are predominately well-drained, rocky, cryic sandy loams, while the grasslands are darker mollics with greater water-holding capacity and organic matter content (Rodriguez and Archer, 2010).

The climate and vegetation of the study site were summarized by Condon (2013), and we summarize her major points here. The study site is semi-arid and seasonally snow-covered. Typically about half of the annual precipitation falls as snow between October and April and the remainder falls during the late summer as rainfall associated with the North American monsoon system (Bowen, 1996). Mean annual temperatures are approximately 3°C. A SNOTEL site 5 km from Redondo Peak averages approximately 750 mm annual precipitation at an elevation of 2794 m (NRCS 2013). At the highest elevations of the study area the forest is comprised of Engelmann spruce (*Picea engelmannii*) and corkbark fir (*Abies lasiocarpa var. arizonica*)

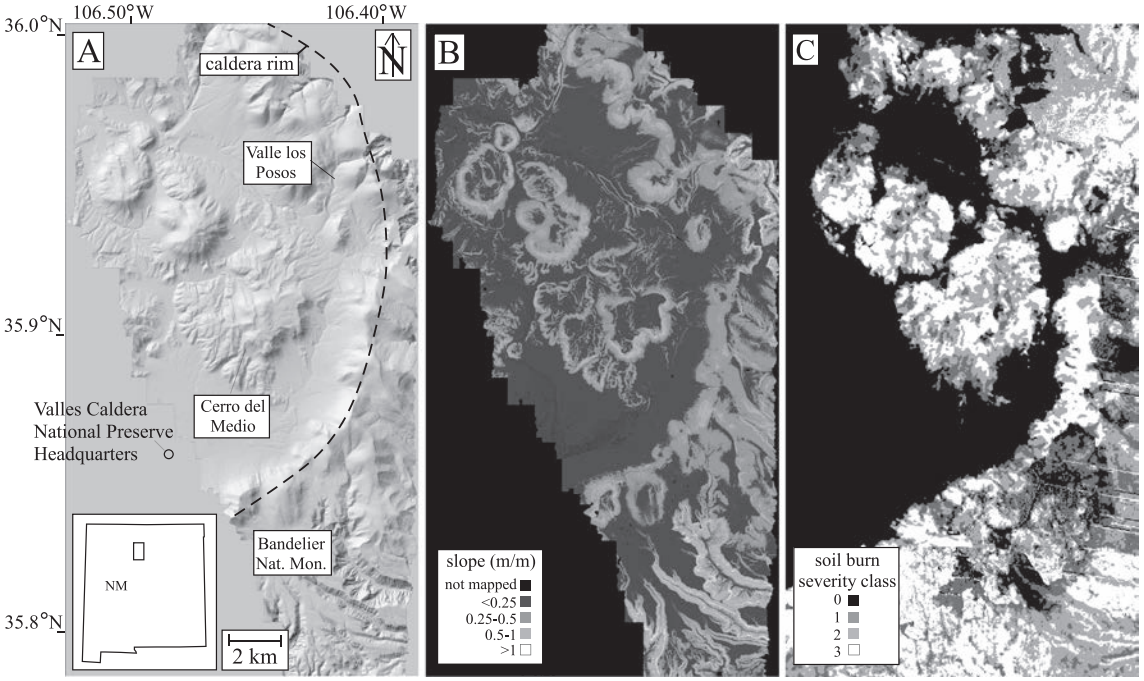

Figure 2. Maps of the study area. (A) Shaded-relief map, showing the locations of important landmarks such as the caldera rim (dashed line), headquarters of the Valles Caldera National Preserve (VCNP), and the locations of the Bandelier National Monument, Cerro del Medio, and Valle los Posos study subareas. Color maps of (B) terrain slope and (C) soil burn severity class (SBSC) (USDA Forest Service, 2011). An SBSC value of zero is used for areas unaffected by fire while 1, 2, and 3 indicate areas of low, medium, and high soil burn severity/erosional potential. This figure is available in colour online at wileyonlinelibrary.com/journal/espl

(Muldavin *et al.*, 2006; Muldavin and Tonne, 2003). Between 2740 and 3040 m, mixed conifer species, such as Douglas fir (*Pseudotsuga menziesii*), white fir (*Abies concolor*) and blue spruce (*Picea pungens*), are interspersed with aspen stands (*Populus tremuloides*). Below 2740 m, the hillslopes are forested with ponderosa pine (*Pinus ponderosa*) and Gambel oak (*Quercus gambelii)*.

The Las Conchas wildfire is one of several large-area and high-severity wildfires to have burned the study site over the last couple of decades. Dendrochronology studies in VCNP have documented a shift in the fire regime from frequent, low-severity wildfires before 1900 to larger, high-severity fires post-1900 (Dewar, 2011). The recurrence interval of wildfires in the pre-1900 era was in the range of two to 25 years based on fire-scar records (Touchan *et al.*, 1996; Dewar, 2011). Large, stand-replacing, high-severity fires have become more common in the modern (post-1900) era with recurrence intervals estimated to be on the order of hundreds of years (Touchan *et al.*, 1996).

Rilling was the most common form of hillslope erosion we observed in areas burned at moderate and high soil burn severity class following the Las Conchas wildfire and subsequent rainstorms (Figure 3). Here we use the term rill to refer to as any incision that occurs on a hillslope or hollow (i.e. portions of the landscape that are divergent, planar, or weakly convergent and that were unincised prior to the wildfire). Rills of approximately 0.5 m depth are common in areas burned at moderate to high severity (Figure 3A), with some rills exceeding 1.5 m depth (Figure 3B). Evidence also exists for thin but widespread hillslope stripping of the uppermost organic-rich layer of the soil together with the litter and duff that had accumulated on top of the soil. In such areas colluvial clasts armor the surface.

Material excavated from hillslopes can be transported in flow events that occur along a continuum from water-dominated floods to debris flows. We made detailed observations of debris-flow-dominated deposits in two drainage basins and their associated piedmonts located on the south side of Cerro del Medio in VCNP (Figure 2A). These deposits can be associated with debris flows based on their poorly sorted, unstratified, and matrix-supported nature as well as the presence of levees (Figure 4; Costa, 1984; Pierson, 2005). Deposit types in the upstream drainage basin varied from small (<1 m in height) levees on the edges of the main incised channel to large (>1 m in height) debris dams behind trees (Figure 4). Clasts within the debris-flow deposits were angular to subangular and very poorly sorted. Clasts on the levees are moderately to very poorly sorted based on Trask sorting coefficients (Trask, 1932) that were everywhere greater than 1.4 and an average of 3.8. The largest clasts within these deposits are approximately 2 m in diameter. The fine-grained matrix found between the clasts included clay to gravel-sized grains and was poorly sorted. Induration of the fine-grained matrix varied throughout the deposits and included loose sand-sized material to indurated silt and clay with small litter particles. Litter ranging in size from pine needles to full trees was commonly intermixed in the debris-flow deposits.

In the two Cerro del Medio drainage basins and their adjacent piedmonts, deposits associated with flood and hyperconcentrated flows (i.e. moderately to well-sorted and stratified deposits, with imbrication present) also occur, especially near the margins of the flows (Figure 5). Figure 5 shows transects of elevation and grain size across the two piedmonts that include debris-flow and hyperconcentrated-flow deposits. Areas of higher elevation that are also convex in shape correspond with debris-flow levees identified in the field. Also shown in Figure 5 are the average and standard deviation of clast intermediate-axis diameters obtained by measuring 10 clasts at each location along the transect. Levee deposits had larger grain sizes and higher standard deviations compared with non-levee locations. Lower standard deviations were interpreted to be an indicator of better sorting. Detailed observations and measurements of the nature of the debris-laden flow deposits were only made in these two Cerro del Medio drainage basins and their adjacent piedmonts, but anecdotally we observed similar characteristics in the large deposits of other highly-impacted portions of the study area.

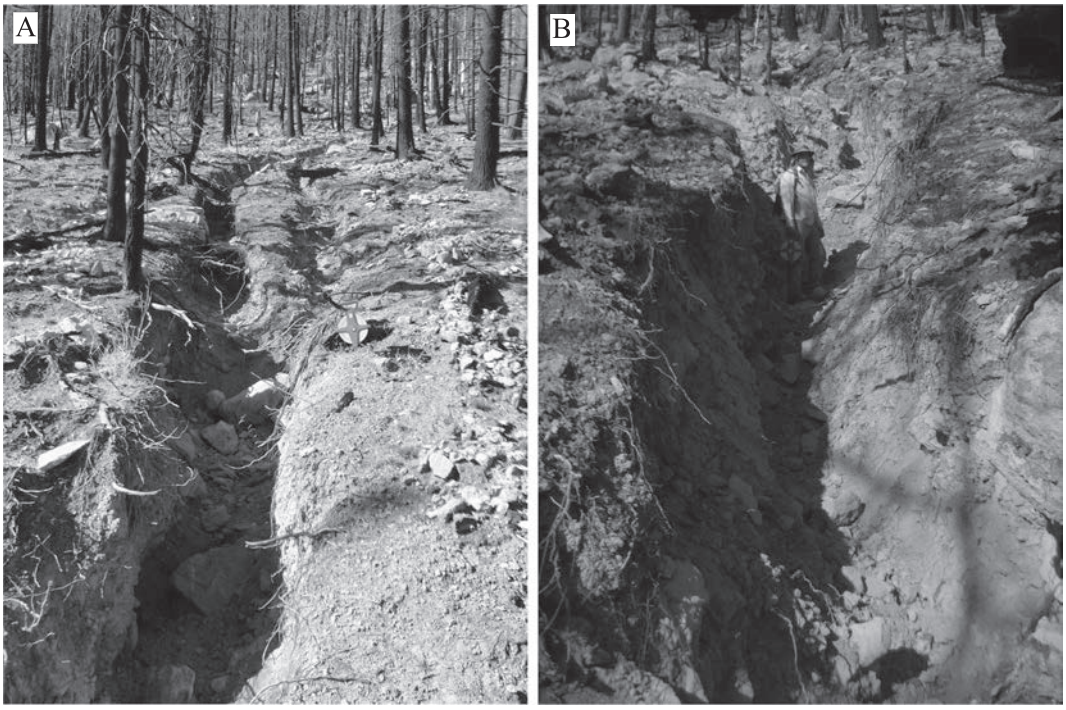

Figure 3. Photographs documenting rilling as an important hillslope erosion mechanism in the Cerro del Medio area. (A) Photograph of a hillslope rill approximately 0.5 m deep (41-cm-tall tape shown for scale, location 368961E, 3973072N, UTM zone 13). Rills of this size are common in hillslope and hollow areas of moderate and high-severity burns throughout the study area. (B) Photograph of an unusually deep rill (1.9-m-tall man for scale) (location 368992E, 3972895N). This figure is available in colour online at wileyonlinelibrary.com/journal/espl

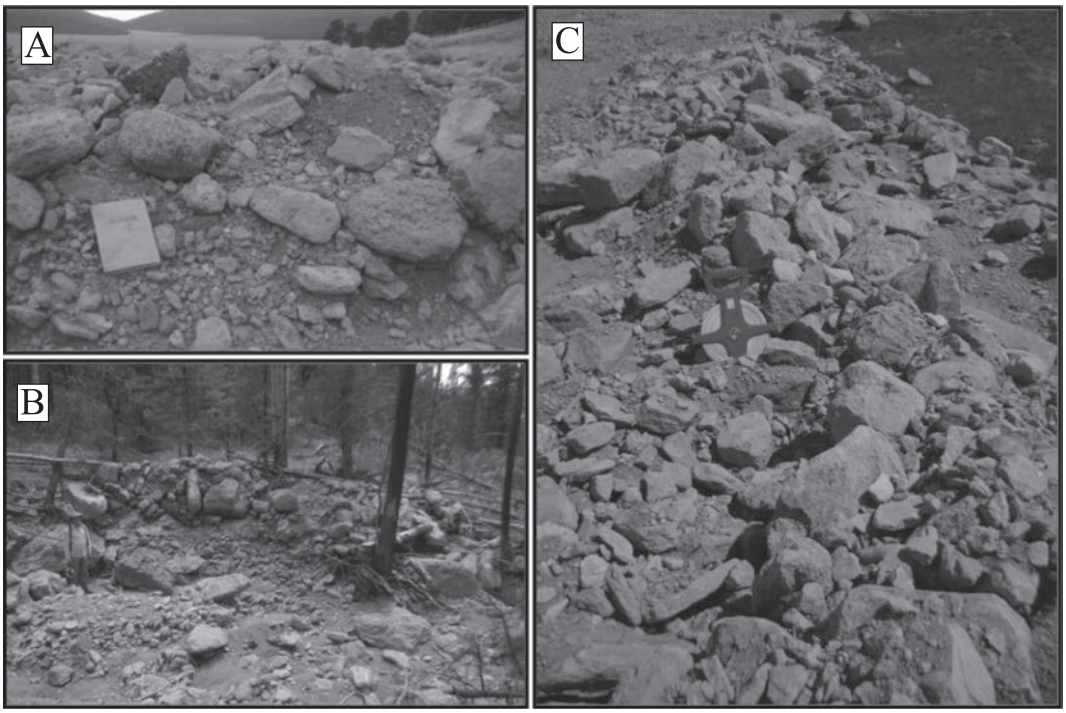

Figure 4. Photographs documenting the debris-flow-dominated nature of the deposits in the Cerro del Medio area. (A) Photograph of a debris-flow-deposit cross-section located on the piedmont draining the south side of Cerro del Medio (20-cm-high notebook for scale). (B) Debris-flow deposit dammed behind collection of trees (1.9-m-tall man for scale). (C) Debris-flow levee located in the proximal area of the piedmont draining the south side of Cerro del Medio (41-cm-high tape for scale). This figure is available in colour online at wileyonlinelibrary.com/journal/espl

In this study we used the US Forest Service's BAER (Burned Area Emergency Response) Soil Burn Severity Class (SBSC) as the metric for quantifying the post-wildfire erosional potential of the landscape (USDA Forest Service, 1995). SBSC maps are produced rapidly after every significant fire event in the United States to determine if fire-caused changes in soil hydrologic function have resulted in an emergency that threatens life, health, property, or critical cultural and natural resources due to flooding, erosion and debris flows. The principal input to SBSC maps is a Burned Area Reflectance Classification (BARC) which uses the dNBR (delta Normalized Burn Ratio) measure of vegetation change derived from the reflectance in bands 4 and

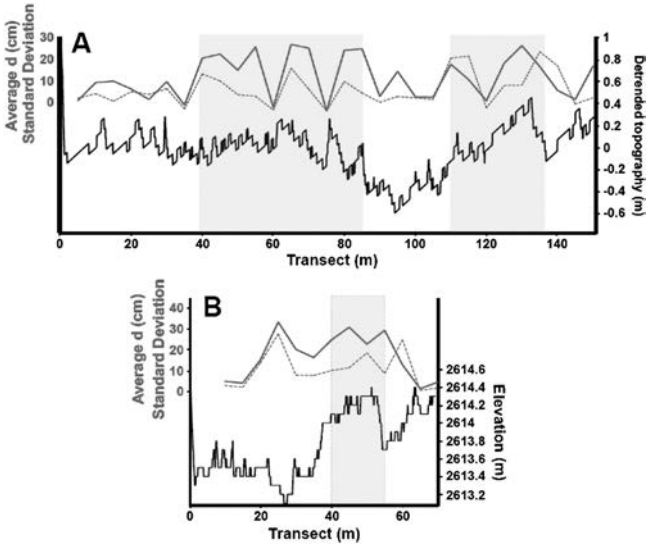

Figure 5. Transects through debris-dominated fan deposits illustrating topography (black line), average diameter of clasts (red line) and standard deviation of clast diameter (dashed red line). Areas identified in the field as extensive debris-flow deposits are marked in gray. The elevation values along the transect illustrated in (A) were detrended to remove the overall east–west slope of the piedmont upon which the debris has been deposited. The transect shown in (B) did not need detrending. This figure is available in colour online at wileyonlinelibrary.com/journal/espl

7 of Landsat TM 30 m/pixel imagery. The BARC map is primarily sensitive to living chlorophyll and the water content of soils and vegetation (Safford *et al.*, 2007). In order to derive a map that relates to erosional potential rather than just vegetation change, the BAER teams use the BARC map as a starting point but augment those data with field visits and data from soils maps and field measurements of the impact of the fire on soils to derive a final BAER SBSC map (Safford *et al.*, 2007). The result of such analyses is a discrete classification (i.e. low, moderate, and high SBSC) rather than a continuous variable because the BAER team is not using a mathematical formula when combining these different data sources to arrive at their class assessments. SBSC classes and/or dNBR data are widely used in quantitative post-fire erosion models (e.g. Gartner *et al.*, 2008; Cannon *et al.*, 2010) because they represent the best widely available measure of post-fire erosional potential. In the Las Conchas wildfire, 35% of the burned area was burned at low severity, 40% was burned as moderate severity, and 25% was burned at high severity (USDA Forest Service, 2011).

Constructing DEMs-of-difference (DoDs) and Associated Sediment Yield Maps for Wildfire-impacted Areas

Airborne LiDAR data (density of 11 to 14 pts m^{-2}) were acquired by the National Center for Airborne Laser Mapping (NCALM) for 197 km^2 of the area burned by the Las Conchas fire one year prior to the fire (June 27–July 8, 2010) and again approximately one year following the fire (May 25–28, 2012). Bare-earth DEMs were constructed by NCALM using the Terrascan software package to distinguish ground from non-ground points, followed by kriging of the ground points. We differenced the co-registered bare-earth DEMs to derive a map of elevation changes, also known as a DEM-of-difference (DoD) (e.g. Wheaton *et al.*, 2010), for every 1 m^2 pixel within the 197 km^2 area of LiDAR coverage. We encountered two registration issues during this process. First, the geoid model used by NCALM differed between the two LiDAR datasets. This was to be expected since it is standard practice for NCALM to use the newest geoid model. Nevertheless, changes in geoid models and other aspects of the projection should be checked carefully by the user when doing LiDAR change-detection work to ensure that elevation differences in the data reflect actual differences in ground-surface elevation. Second, the parameters input to Terrascan used to derive the bare-earth DEMs differed between the two datasets in one portion of the study area. NCALM had modified their input parameters in an attempt to retain steep cliffs in the south-eastern (i.e. Bandelier National Monument) portion of the study area in one LiDAR dataset but not in the other. At our request, NCALM re-ran the Terrascan algorithm using the same Terrascan parameters throughout both datasets to maintain consistency between the two products.

The resulting raw DoD map must be filtered in order to remove changes that are the result of georeferencing errors and other artifacts. The starting point for such filtering is the inherent accuracy of the LiDAR and global positioning system (GPS) instruments at the height above the ground where the data were collected. NCALM estimates this absolute positional accuracy to be in the range of 0.05 to 0.35 m for the two LiDAR datasets used here. Part of this error is associated with the spot size of the laser footprint on the ground. This part of the error is estimated to be $H/5500$ (1σ value), where H is the height of the airplane above the ground. For our LiDAR flights, $H \approx 1000$ m, therefore the 1σ spot-size error is 0.18 m. There is, in addition, a vertical error caused mostly by GPS height error. That error is more difficult to quantify because it depends on instantaneous conditions of satellite communications, but which the manufacturer estimates to be in the range of 0.05 to 0.35 m (Michael Sartori, personal communication, 2012). Dense canopy and especially dense ground cover can also contribute to vertical error by lowering point density and the uncertainty of knowing if any particular measurement was acquired at the bare-earth elevation.

In areas with terrain slopes greater than 45°, vertical errors larger than 0.35 m can occur because a horizontal error of δx translates into a vertical error equal to $\delta x/S$, where S is the slope gradient. This effect was readily apparent in the near-vertical cliffs of the south-eastern (Bandelier National Monument) portion of our study area where the cliff-forming Battleship tuff is exposed. On such near-vertical slopes, a horizontal error of only 0.18 m can result in apparent erosion/deposition of several meters or more. Actual changes of such magnitude are highly unlikely given that cliffs in the study area have little to no regolith cover. To address the potential error associated with cliffs, we eliminated all changes from the DoD in areas steeper than 45° prior to performing any other kind of filtering. This step affects only 1% of the study area.

The DoD map quantifies the erosion/deposition in every pixel. It is also possible to sum the values of erosion/deposition along flow paths to obtain the net erosion upstream from every pixel in the DEM. This value is also the net sediment exported through every pixel in the DEM. This process works by ranking all of the elevations in the DEM from highest to lowest, then starting at the pixel with the highest elevation (i.e. the one with no possible contributing area from upslope) and partitioning the sediment eroded from the bed (if any) into downslope pixels using the multiple flow direction (MFD) routing method of Freeman (1991). The Freeman (1991) method partitions the volume of eroded sediment that enters each pixel into the downstream pixels using the equation

$$f_i = \frac{\max\left(0, S_i^p\right)}{\sum\limits_{j=1..8} \max\left(0, S_j^p\right)}, \quad (1)$$

where f_i is the fraction of incoming volume transferred to the neighboring pixel labeled by i (with i ranging from one to eight), S_i the slope gradient between the central pixel and its neighboring pixels (with downhill slopes defined to be positive, uphill slopes negative), and p is a free parameter. For $p = 1.0$, Freeman (1991) found that flow was preferentially directed towards diagonal pixels. Using a slightly higher value of $p = 1.1$, this effect was eliminated. As such, Freeman (1991) recommended using $p = 1.1$ for best results and we used that value in this study. The algorithm proceeds in rank order from the highest elevation pixel to the lowest elevation pixel in the DEM, summing the amount of erosion/deposition within the pixel being processed with the net erosion from upslope (deposition is treated as negative erosion). The net volume of material eroded upstream from each pixel can then be divided by the upslope contributing area to obtain a sediment yield with units of length (a unit of time is also implicit in this calculation because). Normalizing the sediment volume to compute a yield is useful because it allows drainage basins of different size to be compared to isolate the effects of terrain slope and burn severity. The resulting map is both the net surface elevation decrease upslope from each pixel and the sediment yield Y (expressed as volume per unit area, or length) transported through each pixel. Figure 6 gives an example of the output of this procedure for the Valle los Posos subarea of the study site. We used the MFD method of Freeman (1991) rather than the alternative D8 or D∞ flow routing methods because such schemes force flow to be transported to at most one (D8) or two (D∞) neighboring pixels and hence perform less well in areas of unconfined or distributary flow (such as the divergent portions of hillslopes and the piedmonts of the Valles Caldera) (Pelletier, 2008).

Given the wide range of available estimates of instrument error (i.e. 0.05 to 0.35 m) and the need to use the smallest filter possible so as to retain as much reliable change data as possible, we undertook an analysis designed to estimate the appropriate threshold filter value for our dataset. We used aerial photographs acquired before and one year after (acquisition date May 4, 2012, or just three weeks prior to the second airborne LiDAR flight) the Las Conchas fire in order to identify the areas where significant change took place. Given the large size of the study area, it is not feasible to map every location where significant erosion/deposition took place based on aerial photographs. As such, we focused on three regions (e.g. Valle los Posos, Cerro del Medio, and Bandelier National Monument) where the most significant changes occurred. Maps of where erosion/deposition occurred based on aerial photographic mapping (i.e. manually drawing visible areas of change determined by comparing the before and after photographs) (Figure 7A) were compared with maps of areas of erosion/deposition predicted using different threshold filter values ranging from 0.2 m to 0.4 m (Figures 7B–7D). The maps we obtained when using a threshold filter value of 0.4 m resulted in systematically fewer areas of change than we observed in the aerial photographs. Conversely, the map we obtained when using a threshold filter value of 0.2 m resulted in many areas that we were not able to verify in the aerial photographs. The lowest mismatch between the actual and predicted area of significant change occurred for the threshold filter value of 0.3 m. The results of this analysis, together with the stated accuracy limitations of the LiDAR and GPS instruments, provide a basis for choosing 0.3 m as the optimal value for the threshold filter. It should be noted that even after filtering all changes less than 0.3 m from the DoD there remain some small (but numerous) areas on hillslopes where change is predicted that is difficult to verify in the aerial photographs. For this reason, we also created an alternative, more conservative DoD (described later) that retains only those changes that occur on valley bottoms, i.e. those areas with a contributing area, A, of greater than 0.001 km^2 (Figure 8). An area threshold of 0.001 km^2 was chosen based on a slope–area analysis of the study area (Figure 8). A plot of slope (averaged in logarithmically spaced bins of contributing area) versus contributing area using logarithmic scales exhibits a 'bend' at a drainage area corresponding to the transition from hillslopes and hollows to valley bottoms (Tarboton *et al.*, 1992; Ijjasz-Vasquez and Bras, 1995). Figure 8 establishes that transition is to be 1000 m^2 or 0.001 km^2 in our study area. The purpose of this alternative DoD was to compare the sediment yield map

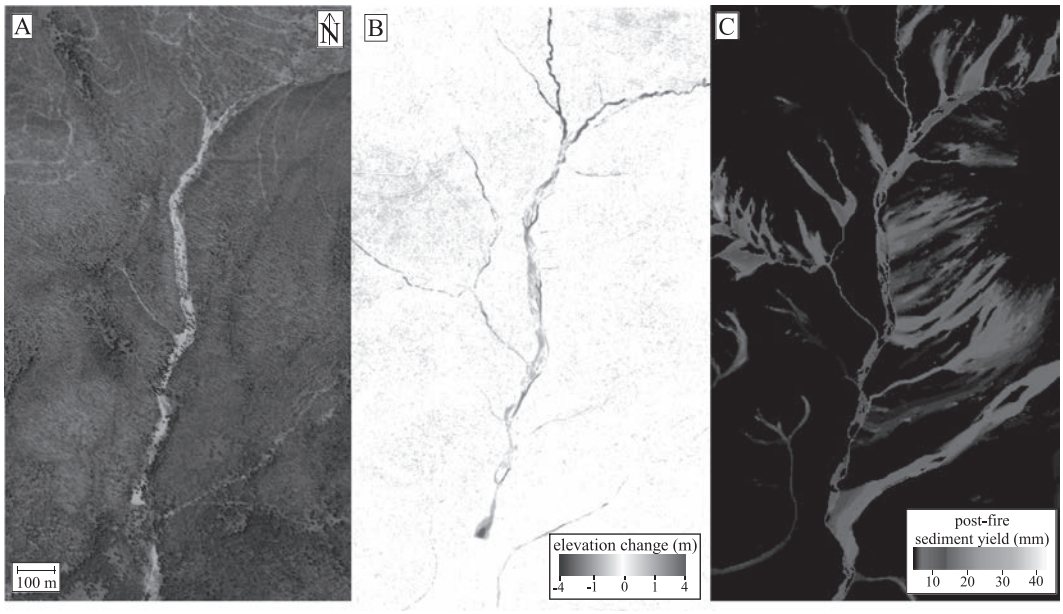

Figure 6. Example of the DEM-of-difference (DoD) and associated sediment yield maps for the Valle los Posos study subarea. (A) Aerial orthophotograph acquired on May 5, 2012. (B) Color map of DoD filtered using magnitude of change, with erosion shown using shades of blue (darker blue represents more erosion) and deposition down using shades of red. (C) Map of sediment yield obtained using the DoD shown in (B) but also filtered by contributing area ($A \geq 0.001$ km^2). Location map for the area depicted in this figure is shown in Figure 9. This figure is available in colour online at wileyonlinelibrary.com/journal/espl

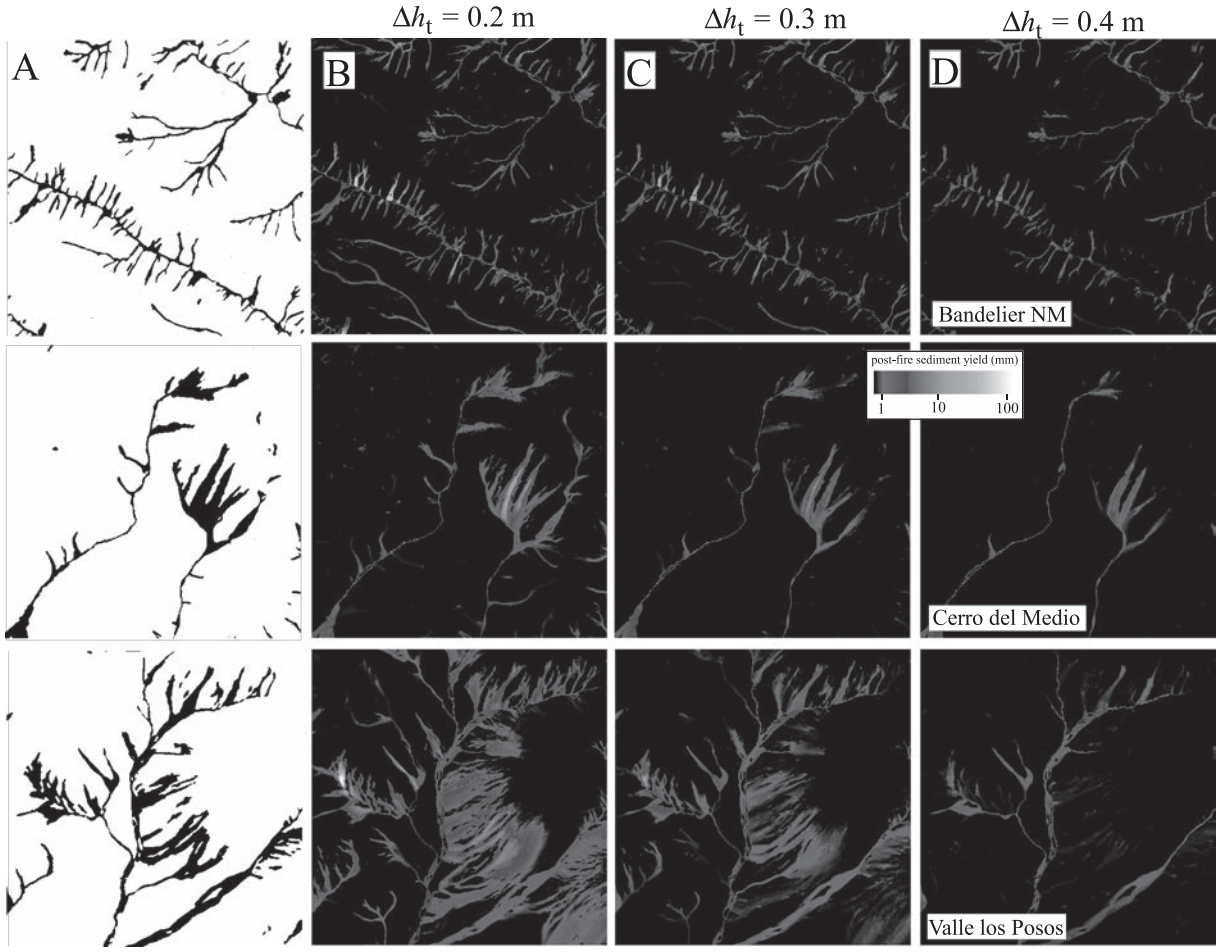

Figure 7. Documentation of the procedure for estimating the appropriate threshold filter value for the DoD. (A) Areas of visible change as determined by a comparison of aerial photographs acquired before and after the Las Conchas wildfire and subsequent rainstorms. (B)–(D) Maps of significant change predicted by computing sediment yields using DoD maps filtered to retain only those changes greater than (B) 0.2 m, (C) 0.3 m, and (D) 0.4 m. Maps of visible change (in A) best match the areas of significant change as predicted by the threshold value of 0.3 m. Maps of predicted change obtained with a threshold value of 0.2 systematically overpredict the area of significant changes while maps obtained with a threshold value of 0.4 underpredict the area of significant changes. This figure is available in colour online at wileyonlinelibrary.com/journal/espl

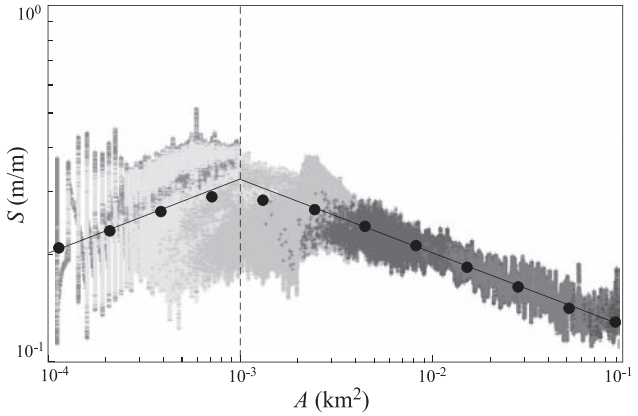

Figure 8. Slope–area plot of the study area, illustrating the transition from hillslopes and hollows (increasing slope with increasing contributing area) to valley bottoms (increasing slope with increasing contributing area) at a drainage area of 0.001 km^2. Filled circles represent the average slope in logarithmically spaced bins of contributing area. Straight lines are not fits to the data but simply highlight the trend of increasing, then decreasing, slope with increasing drainage area characteristics of the two landform types. Colors represent different Strahler orders. This figure is available in colour online at wileyonlinelibrary.com/journal/espl

obtained with this DoD with the predictions of the DoD filtered by magnitude only in order to estimate how much sediment was derived from hillslopes and hollows versus valley bottoms.

Applying the threshold filter with a 0.3 m value removes instances of erosion/deposition that lack sufficient magnitude to be confidently attributed to actual erosion/deposition rather than errors in georeferencing and other artifacts. This filtering ensures that erosional processes that result in relatively thin (but possibly widespread) erosion and deposition will be excluded from the analysis. Other LiDAR datasets could have a smaller detection threshold if the plane were to fly closer to the ground or if the GPS precision were enhanced relative to our datasets.

Analysis of Sediment Yield Data Inferred from DEMs-of-difference (DoDs)

Figure 9A shows the sediment yield map obtained using the DoD which retains only changes $\geq$ 0.3 m in valley bottom areas ($A \geq 0.001$ km^2). Figure 9B shows the sediment yield map obtained when including all areas of the landscape (i.e. filtered only by the magnitude of change). Figure 10 illustrates the relationship between the average sediment volume and contributing area based on the map in Figure 9A. The results in Figure 10 were obtained by averaging exported sediment volumes from all areas (including those where post-fire erosion did not occur) and separately by averaging only those areas where sediment yield is non-zero. The results were similar; when averaging over all areas, sediment volume is a power-law function of contributing area with an exponent of 0.98 ± 0.03 (2σ value),

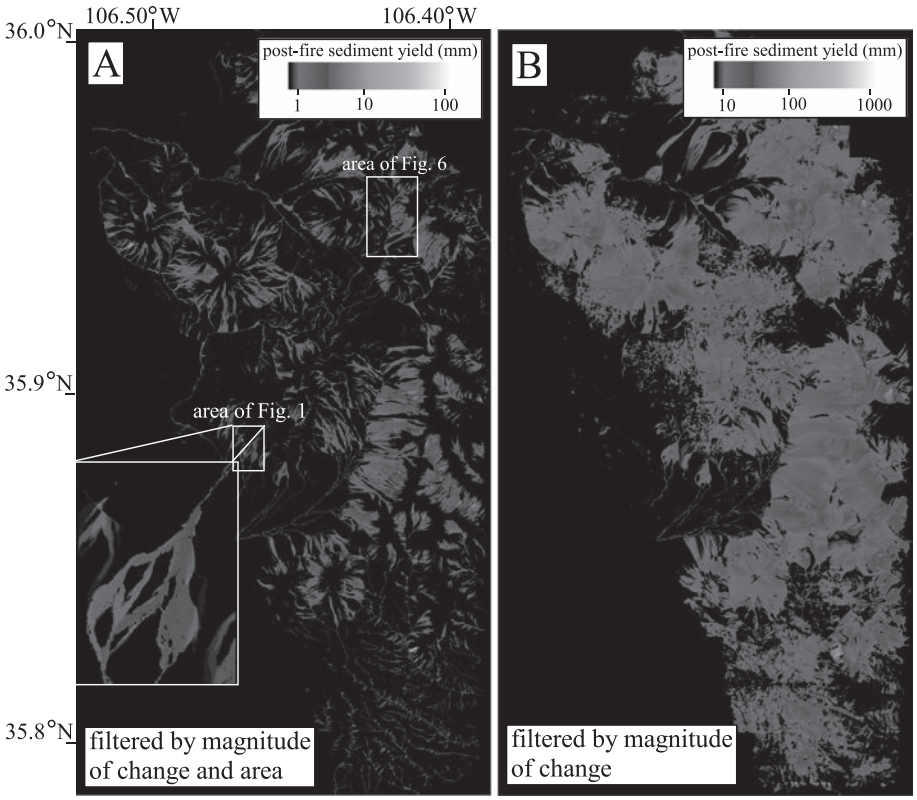

Figure 9. Maps of sediment yield obtained (A) with and (B) without filtering the DoD by contributing area (both are filtered to remove all changes less than 0.3 m). Note that color scale for (B) differs from that of (A). The map in (B) includes sediment sourced from hillslopes, hollows, and valley bottoms while the map in (A) includes only sediment sourced primarily from valley bottoms. This figure is available in colour online at wileyonlinelibrary.com/journal/espl

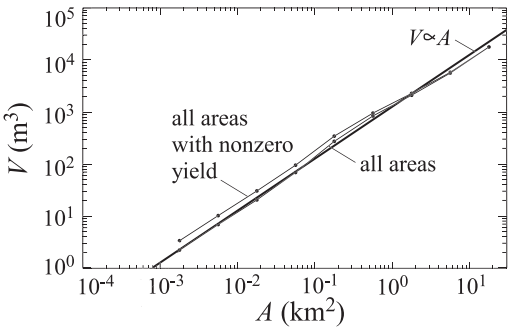

Figure 10. Plot of the average sediment volume as a function of contributing area in drainage basins. Volumes are averaged in 10 logarithmically spaced bins from 0.001 to 20 km^2. Two datasets are shown: the results obtained from averaging only those areas where an erosional event/debris-laden flows occurred (i.e. where sediment volume or yield is non-zero), and another set of averages obtained by averaging all areas. The straight line indicates the trend corresponding to a proportional relationship between sediment volume and contributing area.

while when averaging over only those areas where sediment yield is non-zero, sediment volume is a power-law function of contributing area with an exponent of 0.93 ± 0.08 (2σ value). The fact that volume scales linearly with contributing area (within uncertainty) provides a basis for dividing sediment volume by contributing area to compute maps of sediment yield instead of volume, as in Figure 9. It is useful to work with sediment yield (i.e. volume per unit area) rather than volume because basin size is the largest single factor in determining sediment volume; normalizing for that dominant factor enables the effects of terrain slope and SBSC to be highlighted in the analysis.

Average sediment yields increase steadily and non-linearly with average terrain slope and average SBSC within a drainage basin (Figures 11A and 11B). The map of SBSC for the Las Conchas wildfire used in this analysis is shown in Figure 2B. The effect of average slope and SBSC on average sediment yields can be quantified using

$$Y = aS^b B^c, \tag{2}$$

where Y is the average sediment yield (in millimeters), S is the average slope (in m m^{-1}), B is the average SBSC, and a (in millimeters), b (dimensionless), and c (dimensionless) are coefficients equal to 1.53 ± 0.04 mm, 1.6 ± 0.13, and 1.7 ± 0.23 (uncertainties are 1σ values) for the sediment yield data obtained from the DoD filtered by both magnitude of change and contributing area (Figure 11A), and 4 ± 1 mm, 1.0 ± 0.13, and 1.5 ± 0.24 for the sediment yield data obtained from the DoD filtered by the magnitude of change only (Figure 11B). In Equation (2) we have converted the SBSC from discrete classes of low, moderate, and high burn to numerical values equal to one, two, and three. The values of a, b, and c were obtained from a least-squares multiple linear regression of the log of Y to the logs of S and B. That analysis yielded R^2 coefficients of 0.93 for the data plotted in Figure 11A and 0.87 for the data plotted in Figure 11B. Performing regressions on the average sediment yields rather than all of the data points is appropriate because it weighs all average terrain slope values (within the range of slopes considered, i.e. 0.05 to 1.0) and average SBSC values equally rather than weighing those values that are more common in the landscape (as would be the case if all pixels were used and treated equally in the regression analysis). Figure 11C plots all of the sediment yield data (subsampled by a factor of 30 in order to reduce the number of points to a number that is practical to plot) with an average SBSC in the range of 2.5 to three, illustrating the wide variability in sediment yields within areas of similar average terrain slope and average SBSC. Figure 12 plots the average sediment yield versus drainage basin area.

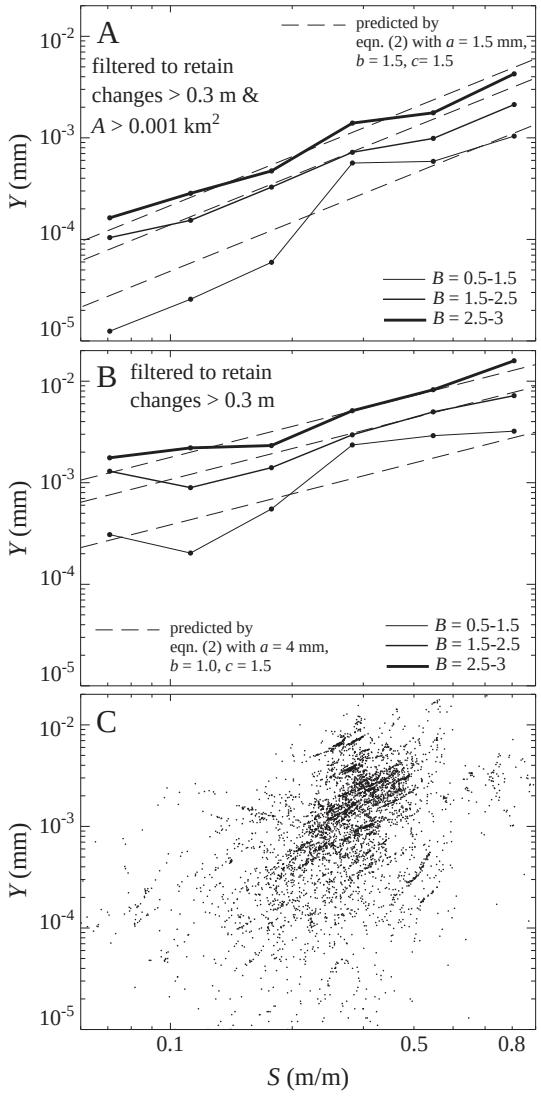

Figure 11. Dependence of average post-wildfire sediment yields, *Y*, on average terrain slope, *S*, and average SBSC, *B*, in drainage basins and comparison of the measurements to the predictions of the empirical model (Equation (2)). Bolder line styles indicate data from more severely burned areas. (A) Relationships among measured and predicted average sediment yields, average terrain slope, and average SBSC using the DoD filtered for both magnitude of change and contributing area. Dashed lines show predictions of Equation (2). Measured data are shown using solid (i.e. un-dashed) lines joining the circles. Note logarithmic scales on both axes. Averaging was performed in six logarithmically spaced bins of slope centered from 0.07 to 0.7 and three bins of average SBSC ($B = 0.5$–1.5, 1.5–2.5 and 2.5–3). (B) Same as (A) except using the DoD filtered for magnitude of change only. (C) Plot of all sediment yields measured in areas of moderate to high average SBSC ($B = 2.5$–3.0), illustrating the large variability about the mean trends illustrated in (A) and (B).

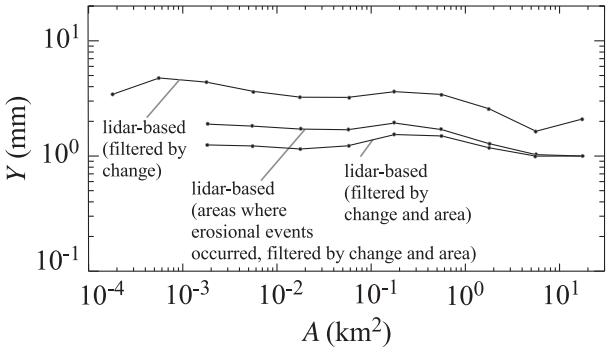

Figure 12. Plot illustrating the dependence of average post-wildfire sediment yield, *Y*, on contributing area, *A*, in drainage basins. Three LiDAR-based measured curves are presented corresponding to yields computed using (1) a DoD filtered by the magnitude of change only, (2) a DoD filtered by the magnitude of change and contributing area (all areas included) and (3) a DoD filtered by the magnitude of change and contributing area with only the areas where erosional events actually occurred included in the analysis. Yields were averaged in 11 logarithmically spaced bins from 0.0001 to 20 km^2 (only nine bins from 0.001 to 20 km^2 for the case of the DoD map filtered by area). This figure is available in colour online at wileyonlinelibrary.com/journal/espl

Discussion

The regression analysis that led to Equation (2) indicates that the sediments transported by debris-laden flows triggered by the Las Conchas wildfire and subsequent rainstorms exhibit yields that vary as a power-law function of average terrain slope and average SBSC within drainage basins with exponents equal to approximately 1.5. The slope exponent is somewhat lower, i.e. 1.0, if sediment from hillslopes and hollows are considered. Our analysis demonstrates that sediment yield may decrease slightly with increasing drainage basin area (Figure 12), but this trend is not statistically significant at the 2σ level (i.e. sediment volume is a power-law function of drainage basin area with best-fit exponents of 0.98 ± 0.03 and 0.93 ± 0.08, hence yield is a power-law function of area with exponents of -0.02 ± 0.03 and -0.07 ± 0.08, respectively). These results are generally consistent with the results of prior studies that used valley-bottom cross-sectional surveys or sediment traps to document the effects of terrain slope and burn severity on sediment volume or yield (described in more detail later). However, there is a strong basis for confidence in the results of this paper given that our measurements are spatially continuous (for changes greater than 0.3 m) over a large (i.e. 197 km^2) area. Equation (2) should provide a useful method for predicting how terrain slope and SBSC control sediment yields in post-wildfire debris-laden flows.

It should be emphasized, however, that the sediment yield data exhibit wide variability about the mean. Figure 11C, for example, shows that areas of similar average terrain slope and SBSC exhibit variations in sediment yield over three orders of magnitude. Similar variability has been reported in other post-wildfire erosion studies. For example, Wagenbrenner and Robichaud (2013) reported sediment yields in drainage basins of similar contributing area, rainfall intensity, etc. that vary over four orders of magnitude. This variability is likely due, in part, to the dependence of post-wildfire erosion processes on small-scale heterogeneity in forcing (e.g. rainfall intensity) and resistance (e.g. soil cohesion) variables that are difficult to quantify. Previous studies have incorporated the effects of unquantified (or unquantifiable) small-scale heterogeneity in the variables that control post-wildfire erosion by introducing a probabilistic element. For example, Gartner *et al.* (2008) and Cannon *et al.* (2010) used one equation to predict the probability of a significant debris flow occurring within a wildfire-affected drainage basin and a second equation to predict the volume of sediment exported from a drainage basin if a significant debris flow (i.e. one measurable using valley-bottom cross-sectional surveys) occurs. In their approach, much of the variability in sediment yields is represented by the probability-of-occurrence equation. Equation (2), in contrast, includes the average sediment yield from areas with and without debris flows readily observed and measured in the field, hence the variability about the mean is large.

In this paper we presented two alternative maps for sediment yield, i.e. one based on a DoD filtered only by the magnitude of change only (values ≥ 0.3 m are retained) and another filtered by both the magnitude of change and contributing area (values ≥ 0.3 m and $A \geq 0.001$ km^2 are retained). Average sediment

yields obtained by filtering the DoD by the magnitude of change only (Figure 9B) are approximately three times larger than those obtained using the DoD filtered by using both the magnitude of change and contributing area (illustrated in Figure 9A). This result suggests that the majority of sediment exported from drainage basins in our study area was derived from hillslopes and hollows rather than from valley bottoms. We regard the map based on DoD filtering by both magnitude of change and contributing area as the most conservatively reliable map in the sense that we have high confidence that nearly all of the measured change actually occurred. We can be less confident that all or nearly all of the change in the map shown in Figure 9B (which includes hillslopes and hollows as sediment sources) actually occurred because it is more difficult to visually confirm small topographic changes everywhere on hillslopes over a large study area due to the fact that erosion often occurs in narrower zones and because forest cover tends to obscure changes on hillslopes more so than in valley bottoms. Given that upland landscapes are typically ~99% hillslopes, even if potentially erroneous values occur with a relatively low density on hillslopes they can collectively add up to a significant proportion of the total. There are, however, two reasons to be confident that much of the yield measured on hillslopes and hollows and included in Figure 9B actually occurred. First, Figure 3 demonstrates that significant hillslope erosion occurs in our study area that is well above the change detection threshold for airborne LiDAR. Second, Figure 11B shows that when hillslopes are included in the sediment yield analysis, the resulting data retain highly significant correlations with average terrain slope and SBSC. If the DoD were generally unreliable on hillslopes even above the 0.3 m threshold, we would expect poor or non-existent correlations with average terrain slope and SBSC.

Measurement of post-wildfire sediment transport using airborne-LiDAR change detection has some clear limitations. In addition to uncertainties associated with the change detection threshold, airborne LiDAR data is expensive to acquire. As such, the temporal resolution associated with airborne LiDAR data will likely remain low relative to simpler, less-expensive methods (such as sediment traps) which provide data with very limited spatial coverage but can resolve individual rainstorms. The limitations of airborne-LiDAR change detection and the associated empirical equation we developed (Equation (2)) are somewhat mitigated, however, when combined with the data and associated empirical equation developed by Wagenbrenner and Robichaud (2013) using sediment traps. These authors quantified how post-wildfire sediment yields derived from bedload transport depend on drainage basin area, percent ground cover, event-based rainfall intensity, and time following a wildfire. Their empirical equation predicts sediment yield (expressed in Mg ha^{-1}) between spatial scales of 20 m^2 to 1.17 km^2 based on input data for percent ground cover, C_n, storm intensity I_i (mm h^{-1}), drainage basin area A (m^2), and a regression coefficient for each year following the wildfire, b_n, as

$$Y = 10^{-0.018C_n+0.042I_i+b_n}A^{-0.21}. \quad (3)$$

The mean value for the coefficient $10^{-0.018C_n+0.042I_i+b_n}$ for all wildfires and all terrain slopes was 3.80 Mg ha^{-1} m$^{0.21}$ for the first year following a wildfire event. Assuming a soil density of 1500 kg m^{-3}, Equation (3) predicts one-year sediment yields in the range of 1.4 to 5.9 mm for drainage basins ranging in area from 0.001 km^2 to 1 km^2, i.e. broadly consistent with the values obtained in this study. Equation (2) nicely compliments Equation (3) in that Equation (2) includes effects neglected in Equation (3) (e.g. terrain slope) while Equation (3) includes effects neglected in Equation (2) (e.g. rainfall intensity). That said, it is unclear without further research (e.g. a comparison of sediment yield measurements obtained using sediment traps and airborne LiDAR change detection at the same site) whether Equations (2) and (3) can be combined to form a single predictive equation given the different measurement techniques employed and the different sediment transport processes captured by those methods. Moreover, the two studies reach somewhat different conclusions on a few points. For example, Wagenbrenner and Robichaud (2013) reported a weak dependence on drainage basin area (Equation (3)) while we report no statistically significant decline in sediment yield with increasing drainage basin area. It is difficult to compare our results with those of Wagenbrenner and Robichaud (2013) with regard to burn severity since they used percent ground cover rather than SBSC as their measure of burn severity and recovery. Clearly a higher burn severity class correlates broadly with lower percent ground cover, hence the two empirical equations make qualitatively similar predictions with respect to ground cover/burn severity. There is a potential advantage in using SBSC in predictive equations for post-wildfire erosion since SBSC incorporates vegetation density before the fire and is readily measured by BAER teams shortly following all major US wildfires. In contrast, estimates of ground cover generally require point-based field measurements by individual investigators.

Our conclusion that sediment was sourced primarily from hillslopes and hollows potentially differs from the conclusions of Santi *et al.* (2008), who measured rill erosion from hillslopes in burned areas of the south-western United States and found that rill erosion accounted for an average of only 3% of the total post-fire erosion in the drainage basins they studied. This finding is consistent with similarly low percentages of rill erosion on hillslopes measured in the Colorado Front Range by Moody and Martin (2001). There are at least three possible reasons for this apparent discrepancy. First, our study and those of Moody and Martin (2001) and Santi *et al.* (2008) all consider different study areas and wildfire events. Individual events can and do differ in the relative importance of hillslopes as sediment sources, and it may be that the Las Conchas wildfire is an outlier in this regard. Second, Santi *et al.* (2008) considered rills and side channels separately in their analysis but it may be that some of their side channels are analogous to our hillslope rills. In their Figure 9, for example, they show a debris flow that occurred in a side channel that appears to be a relatively planar or weakly convergent hillslope or hollow. If side channels and rills are considered together, Santi *et al.* (2008) found that such areas produced a large percentage (i.e. between 8% and 66%, depending on the study site) of the total sediment exported from the landscape. A third possibility is that some of the erosion/deposition values we measured that were greater than 0.3 m on hillslopes and in hollows were, in fact, caused by georeferencing and other artifacts.

Gartner *et al.* (2008) and Cannon *et al.* (2010) developed what is perhaps the most widely used model for predicting the probability and volume of debris flows in wildfire-impacted drainage basins. Indeed, the Gartner–Cannon model was used by Tillery *et al.* (2011) to predict debris flows in our study area shortly following the Las Conchas fire. Unfortunately, it is difficult to compare the empirical equation we developed in this paper with the Gartner–Cannon model because their model applies only to debris flows. Our field observations indicate that, while debris flows are likely the dominant type of erosional events in our study area, flood and hyperconcentrated flow deposits are also present.

Conclusions

Our results demonstrate that airborne LiDAR datasets acquired before and after wildfires and subsequent rainstorms can be

useful in constructing high-resolution, spatially continuous maps of post-wildfire sediment yields over large areas. Such maps are limited, however, in that they can only resolve relatively large magnitudes (i.e. ≥ 0.3 m for the LiDAR data products used in this study) of erosion and deposition. Using such a map for the Las Conchas wildfire and subsequent rainstorms that occurred one year after the wildfire, we showed that the average sediment yield from a drainage basin is a power-law function of the average terrain slope and SBSC of the drainage basin. Our empirical Equation (2) should provide a useful tool, together with empirical equations developed by other researchers (e.g. Wagenbrenner and Robichaud, 2013), for predicting post-wildfire sediment yields.

Acknowledgements—The authors thank NSF for funding the post-fire LiDAR data acquisition (through a supplementary award to NCALM) and for funding the UA Critical Zone Observatory via NSF Award #0724958. The authors also thank NCALM for collecting the LiDAR data and producing bare-earth DEMs and Michael Sartori for helpful discussions regarding the positional accuracy of airborne LiDAR data products. The authors wish to thank editor Stuart Lane, the associate editor, John Moody, and two anonymous reviewers for comments which helped us improve the manuscript.

References

Allen CD, Macalady AK, Chenchoun H, Bachelet D, McDowell N, Venntier M, Kitzberger T, Rigling A, Breshears DD, Hoggm EH, Gonzalez P, Fensham R, Zhang Z, Castro J, Demidova N, Lim J-H, Allard G, Running SW, Semerci A, Cobb N. 2010. A global overview of drought and heat-induced tree mortality reveals emerging climate change risks for forests. *Forest Ecology and Management* **259**: 660–684. DOI. 10.1016/j.foreco.2009.09.001

Bowen BM. 1996. Rainfall and climate variation over a sloping New Mexico plateau during the North American monsoon. *Journal of Climate* **9**(12): 3432–3442.

Cannon SH, Gartner JE, Rupert MG, Michael JA, Rea AH, Parrett C. 2010. Predicting the probability and volume of postwildfire debris flows in the intermountain western United States. *Geological Society of America Bulletin* **122**: 127–144.

Condon KE. 2013. Quantifying Catchment-Scale Particulate Organic Matter (POM) Loss Following Fire, Relative to Background POM Fluxes. Unpublished M.S. Thesis, University of Arizona, Tucson, Arizona; 145 p.

Costa JE. 1984. Physical geomorphology of debris flows. In *Development and Application of Geomorphology*, Costa JE, Fleisher PJ (eds). Springer-Verlag: Berlin; 268–316.

Dewar JJ. 2011. Fire History of Montane Grasslands and Ecotones of the Valles Caldera, New Mexico, USA, Master's Thesis. University of Arizona; Tucson, AZ, 193 pp.

Freeman GT. 1991. Calculating catchment area with divergent flow based on a rectangular grid. *Computers & Geosciences* **17**: 413–422.

Gartner JE, Cannon SH, Santi PM, DeWolfe VG. 2008. Empirical models to predict the volumes of debris flows generated by recently burned basins in the western U.S. *Geomorphology* **96**: 339–354.

Goff F, Gardner JN, Reneau SL, Goff CJ. 2006. *Preliminary Geologic Map of the Redondo Peak Quadrangle, Sandoval County, New Mexico*, New Mexico Bureau of Geology and Mineral Resources Open-File Digital Geologic Map OF-GM 111. New Mexico Bureau of Geology and Mineral Resources: Socorro, NM.

Ijjasz-Vasquez EJ, Bras RL. 1995. Scaling regimes of local slope versus contributing area in digital elevation models. *Geomorphology* **12**: 299–311.

Keane R, Ryan K, Veblen T, Allen C, Logan J, Hawkes B. 2002. Cascading Effects of Fire Exclusion in Rocky Mountain Ecosystems. A Literature Review, USDA Forest Service, Rocky Mountain Research Station, General Technical Report RMRS-GTR-91. USDA Forest Service: Washington, DC; 24 pp.

Loomis J, Wohlgemuth PW, Gonzales-Caban A, English D. 2003. Economic benefits of reducing fire-related sediment in southwestern fire-prone ecosystems. *Water Resources Research* **39**: 1260. DOI. 10.1029/2003WR002176

Miller JD, Safford HD, Crimmins M, Thode AE. 2009. Quantitative evidence for increasing forest fire severity in the Sierra Nevada and Southern Cascade Mountains, California and Nevada, USA. *Ecosystems* **12**: 16–32.

Moody JA, Martin DA. 2001. Initial hydrologic and geomorphic response following a wildfire in the Colorado Front Range. *Earth Surface Processes and Landforms* **26**: 1049–1070.

Muldavin E, Tonne P. 2003. A vegetation survey and preliminary ecological assessment of Valles Caldera National Preserve. New Mexico: Report for Cooperative Agreement No. 01CRAG0014, University of New Mexico, Albuquerque.

Muldavin E, Tonne P, Jackson C, Neville T. 2006. A vegetation map of the Valles Caldera National Preserve. New Mexico: Final Report for Cooperative Agreement No. 01CRAG0014, University of New Mexico, Albuquerque.

Natural Resources Conservation Service (NRCS). 2013. National Water and Climate Center, Quemazon SNOTEL Site 708. Digital data available at http://www.wcc.nrcs.usda.gov/nwcc/site?sitenum=708&state=nm.

Pelletier JD. 2008. *Quantitative Modeling of Earth Surface Processes*. Cambridge University Press: Cambridge.

Pierson TC. 2005. *Distinguishing between Debris Flows and Floods from Field Evidence in Small Watersheds*, US Geological Survey Fact Sheet 2004–3142. US Geological Survey: Reston, VA; 4.

Rhoades CC, Entwistle D, Butler D. 2011. The influence of wildfire extent and severity on streamwater chemistry, sediment and temperature following the Hayman Fire, Colorado. *International Journal of Wildland Fire* **20**: 430–442.

Rodriguez M, Archer V. 2010. *Valles Caldera National Preserve: Soils Existing Condition Report*. Valles Caldera National Preserve: Jemez Springs, NM.

Safford HD, Miller J, Schmidt D, Roath B, Parsons A. 2007. BAER soil burn severity maps do not measure fire effects to vegetation: a comment on Odion and Hanson (2006). *Ecosystems* **11**: 1–11. DOI. 10.1007/s10021-007-9094-z

Santi PM, deWolfe VG, Higgins JD, Cannon SH, Gartner JE. 2008. Sources of debris flow material in burned areas. *Geomorphology* **96**: 309–319.

Tarboton DG, Bras RL, Rodriguez-Iturbe I. 1992. A physical basis for drainage density. *Geomorphology* **5**: 59–76.

Tillery AC, Darr MJ Cannon SH, Michael JA. 2011. *Postwildfire Preliminary Debris Flow Hazard Assessment for the Area Burned by the 2011 Las Conchas Fire in North-central New Mexico*, US Geological Survey Open-File Report 2011–1308. US Geological Survey: Reston, VA.

Touchan R, Allen CD, Swetnam TW. 1996. Fire history and climatic patterns in ponderosa pine and mixed-conifer forests of the Jemez Mountains, northern New Mexico. In *Fire Effects in Southwestern Forests: Proceeding of the Second La Mesa Fire Symposium, Los Alamos, New Mexico*, Allen CD (ed.). USDA Forest Service, Rocky Mountain Forest and Range Experiment Station: Fort Collins, CO; 215.

Trask PD. 1932. *Origin and Environment of Source Sediments of Petroleum*. Gulf Publishing: Houston, TX; 323.

USDA Forest Service. 1995. *Burned Area Emergency Rehabilitation Handbook*, US Department of Agriculture Forest Service Handbook 2509.13, Amendment No. 2509.13-95-7. USDA Forest Service: Washington, DC.

USDA Forest Service. 2011. *Las Conchas Fire Burn Severity Map*. US Department of Agriculture Forest Service, Santa Fe National Forest: Santa Fe, NM.

Wagenbrenner JW, Robichaud PR. 2013. Post-fire bedload sediment delivery across spatial scales in the interior western United States. *Earth Surface Processes and Landforms*. DOI. 10.1002/esp.3488

Westerling AL, Hidalgo HG, Cayan DR, Swetnam TW. 2006. Warming and earlier spring increase western U.S. forest wildfire activity. *Science* **313**: 940–943.

Wheaton JM, Brasington J, Darby SE, Sear D. 2010. Accounting for uncertainty in DEMs from repeat topographic surveys: improved sediment budgets. *Earth Surface Processes and Landforms* **35**: 136–156.

Williams AP, Allen CD, Millar C, Swetnam TA, Michaelsen J, Still CJ, Leavitt SW. 2010. Forest responses to increasing aridity and warmth in southwestern North America. *Proceedings of the National Academy of Sciences of the USA* **107**: 21289–21294.

